JOURNAL OF GEOPHYSICAL RESEARCH: SPACE PHYSICS, VOL. 118, 1972–1983, doi:10.1002/jgra.50229, 2013

A statistical study of proton precipitation onto the Martian upper atmosphere: Mars Express observations

C. Diéval,[1,2] G. Stenberg,[1] H. Nilsson,[1] and S. Barabash[1]

Received 23 January 2013; revised 8 March 2013; accepted 11 March 2013; published 6 May 2013.

[1] Due to the small size of the Martian magnetic pile-up region, especially at the subsolar point, heated protons with high enough energy can penetrate the induced magnetosphere boundary without being backscattered, i.e., they precipitate. We present a statistical study of the downgoing ~keV proton fluxes measured in the Martian ionosphere by the Analyzer of Space Plasma and Energetic Atoms experiment onboard the Mars Express spacecraft. We find that on the dayside, the events of proton penetration occur during 3% of the observation time; the precipitation is an intermittent phenomenon. The proton events carry on average ~0.2% of the incident solar wind flux. Therefore, the induced magnetosphere is an effective shield against the magnetosheath protons. The events are more frequent during fast solar wind conditions than during slow solar wind conditions. The sporadic proton penetration is thought to be caused by transient increases in the magnetosheath temperature. The precipitating flux is higher on the dayside than on the nightside, and its spatial deposition is controlled by the solar wind convective electric field. The largest crustal magnetic anomalies tend to decrease the proton precipitation in the southern hemisphere. The particle and energy fluxes vary in the range 10^4–10^6 cm^{-2} s^{-1} and 10^7–10^9 $eVcm^{-2}$ s^{-1}, respectively. The corresponding heating for the dayside atmosphere is on average negligible compared to the solar extreme ultraviolet heating, although the intermittent penetration may cause local ionization. The net precipitating proton particle flux input to the dayside ionosphere is estimated as $1.2 \cdot 10^{21}$ s^{-1}.

Citation: Diéval, C., G. Stenberg, H. Nilsson, and S. Barabash (2013), A statistical study of proton precipitation onto the Martian upper atmosphere: Mars Express observations, *J. Geophys. Res. Space Physics*, *118*, 1972–1983, doi:10.1002/jgra.50229.

1. Introduction

[2] Mars does not have a global planetary magnetic field. As a consequence, the solar wind flow, carrying the interplanetary magnetic field (IMF), can directly encounter the Martian ionosphere. The moving IMF generates currents in this conductive obstacle. The magnetic field associated with the currents diverts the solar wind. A magnetic barrier (magnetic pile-up region) is formed through the superposition of the induced magnetic fields and the partial diffusion of the IMF lines into the ionosphere. The IMF lines drape around the dayside of the planet, slip over the terminator, and extend into a magnetotail on the nightside. An induced magnetosphere forms. Localized crustal magnetic anomalies, mainly present in the southern hemisphere, locally modify the Mars-solar wind interaction [e.g., *Acuña et al*., 1998, 1999]. The reader can refer to for example the review paper of *Nagy et al*. [2004].

[3] The magnetic barrier is delimited from below by the photoelectron boundary (PEB) and from above by the induced magnetosphere boundary (IMB). The PEB marks the presence of ionospheric photoelectron with energy peaks in the energy range 20–24 and at 27 eV [*Frahm et al*., 2006], generated by photoionization of atmospheric CO_2 and O by the solar 304 Å He line. We refer to the CO_2 photoelectron line. The IMB is a boundary that is analogous to a magnetopause where the magnetic field strongly increases and the solar wind flux terminates.

[4] However, hybrid models (which treat the ions as particles and the electrons as a massless charge-neutralizing fluid) predict that the IMB is permeable to heated solar wind protons with high enough energies [*Brecht*, 1997; *Kallio and Janhunen*, 2001; *Diéval et al*., 2012a, 2012b]. This situation arises because in the subsolar magnetosheath, the hot plasma (proton temperature of 40–60 eV [*Fränz et al*., 2006]) includes populations of protons with high energies and large gyroradii $mv_\perp/qB$. B is the magnetic field strength, m and q are respectively the mass and charge of the proton. $v_\perp$ is the proton velocity perpendicular to the magnetic field. These high energy protons can thus penetrate the magnetic barrier without being deflected away and can enter the upper atmosphere. Modeling studies demonstrate that the precipitating solar wind protons contribute to ionizing and heating the atmosphere, and they are neutralized by charge exchange reactions with the atmospheric neutrals

[1]Swedish Institute of Space Physics, Kiruna, Sweden.
[2]Division of Space Technology, Department of Computer Science, Electrical and Space Engineering, Luleå University of Technology, Kiruna, Sweden.

Corresponding author: C. Diéval, Swedish Institute of Space Physics, Box 812, SE–98128, Kiruna, Sweden. (catherine@irf.se)

2169-9380/13/10.1002/jgra.50229

[*Kallio and Barabash*, 2001; *Kallio and Janhunen*, 2001; *Shematovich et al*., 2011]. Most of the precipitating protons are lost between 100 and 150 km altitude, where they experience charge exchange reactions with the atmospheric CO_2, O, and N_2. The cross-sections of these reactions for keV protons can be found in *Shematovich et al*. [2011], *Stebbings et al*. [1964], and *McNeal and Clark* [1969], respectively.

[5] Observations of solar wind proton entries into the dayside Martian atmosphere have been reported in the literature [*Lundin et al*., 2004; *Diéval et al*., 2012b]. The study of *Diéval et al*. [2012b] is a detailed analysis of the data from one orbit of the Mars Express (MEX) spacecraft, with observations of downgoing proton fluxes in the dayside ionosphere. Using hybrid simulations, the authors have determined that the measured protons originate both from the solar wind and the upper neutral hydrogen atmosphere (hydrogen exosphere). They attributed the observed proton precipitation to the gyroradius effect, meaning that the gyroradius size becomes comparable to the size of the local magnetic barrier.

[6] However, there is no statistical study available so far providing observations of proton precipitation or any investigation of proton precipitation on the nightside. Hybrid models predict proton precipitation on the nightside and show significant atmospheric effects there in the absence of solar radiation [*Brecht*, 1997; *Kallio and Janhunen*, 2001; *Diéval et al*., 2012a]. The purpose of this paper is to make an observational statistical study of the downgoing proton fluxes at low altitude around Mars, both on the dayside and on the nightside. We use data from the Analyzer of Space Plasma and Energetic Atoms (ASPERA-3) experiment onboard MEX. The paper compares the observations with model predictions.

[7] Section 2 describes the instruments used in this study and the data selection, and it presents an example of proton penetration. Section 3 presents the spatial distribution and characteristics of the precipitating protons. Section 4 investigates the dependence of the precipitation on the solar wind conditions, the IMF direction, and the crustal magnetic anomalies. Section 5 treats the net flux of the precipitation. Finally, section 6 discusses the results.

2. Instrumentation, Data Selection, and Methods

[8] ASPERA-3 is an instrument package designed to study the interaction between the solar wind and the Martian atmosphere [*Barabash et al*., 2006]. It includes the ELectron Spectrometer (ELS), the Ion Mass Analyzer (IMA), and two energetic neutral atom sensors. We used data from the ELS and IMA sensors, which are described in more detail below.

[9] The ELS instrument measures the two-dimensional distributions of the electron flux in the energy range of 5 eV to 15 keV ($\Delta E/E = 8\%$) with a field of view of $4^\circ \times 360^\circ$ divided into 16 azimuth sectors. The time resolution used in this study is 4 s. The IMA instrument consists of an electrostatic deflection system, followed by a top-hat electrostatic energy analyzer and a magnetic mass analyzer. The IMA sensor measures the fluxes of different ion species with m/q resolution (m and q being the ion mass and charge), including H^+, He^{2+}, O^+ and molecular ions with $20 < m/q < 80$. The measurements are in the energy range 10 eV/q to 36 keV/q for all ion species except H^+, where the lower energy limit is ~1.2 keV for the intermediate postacceleration level (PAC). The PAC voltage serves to vary the mass resolution of the instrument (see details in *Barabash et al*. [2006]). Low values of PAC increase the mass resolution but result in protons with energy < 2 keV hitting the walls of the instrument (due to a small gyroradius), preventing their detection. The highest PAC level is needed for measuring protons with energies below 1 keV. With a time resolution of 12 s, IMA gives a two-dimensional measurement of the ion fluxes (16 azimuth sectors) for all energies. For this study, electrostatic sweeping provides $\pm 45^\circ$ coverage out of the plane of the aperture (scanning in elevation angle) and a complete distribution with a field of view of $90^\circ \times 360^\circ$ is produced in 192 s (an IMA scan).

[10] Both ELS and IMA have other operational modes that are not used in this study. For our statistical study, we use electron and ion data taken from February 2004 to April 2011. The analysis was conducted for the solar minimum. Two new energy tables were uploaded for IMA, one in May 2007 and the other in November 2009. We have not used data from these two months. In addition, we have excluded data from periods when the elevation scanning was off.

[11] The analysis covers altitudes ≤ 2000 km. The electron data are used to identify the plasma regions. An inbound IMB crossing is identified by a sharp decrease in suprathermal (i.e., 40–300 eV in energy) electron fluxes. An inbound PEB crossing is identified by the appearance of the CO_2 photoelectrons [*Frahm et al*., 2006]. This feature marks the entry into the ionosphere. On the dayside, we have manually searched for proton fluxes in the presence of the photoelectrons that are not accompanied by magnetosheath-like electrons to ensure that the spacecraft is in the dayside ionosphere. On the nightside, the photoelectrons are less frequently observed, and there we just require the proton fluxes to be located below the IMB. We have checked that a proton flux exists in downgoing directions during these IMA scans (we want precipitating particles) during at least 24 s. Then, we have integrated the downward proton flux from a 3-D distribution (of time resolution = 192 s), to obtain a total downward flux of the "event" of proton precipitation. We have finally discarded cases where the proton mass channel of IMA is severely contaminated by ultraviolet (UV) radiation and alpha particles; these cases are referred to as invalid data.

[12] All measurements by Mars Express are made above the exobase, which is located at approximately 180 km altitude at the solar minimum. Incoming protons that arrive at the exobase undergo collisions with the atmospheric neutrals and lose energy. These protons are neutralized by charge exchange reactions at lower altitude and are considered lost in the atmosphere [*Kallio and Barabash*, 2000]. In this study, we have assumed that all precipitating proton fluxes reach the exobase and deposit their mass and energy further down.

[13] Figure 1 gives an example of the precipitating protons observed by MEX on 4 October 2005 in the subsolar region at solar zenith angles (SZA) <50°. The time interval is 1540–1640 UT. The pericenter is reached at 1612 UT at ~270 km altitude (Figure 1a). The magnetosheath is recognized by the high fluxes of 40–300 eV electrons (Figure 2b).

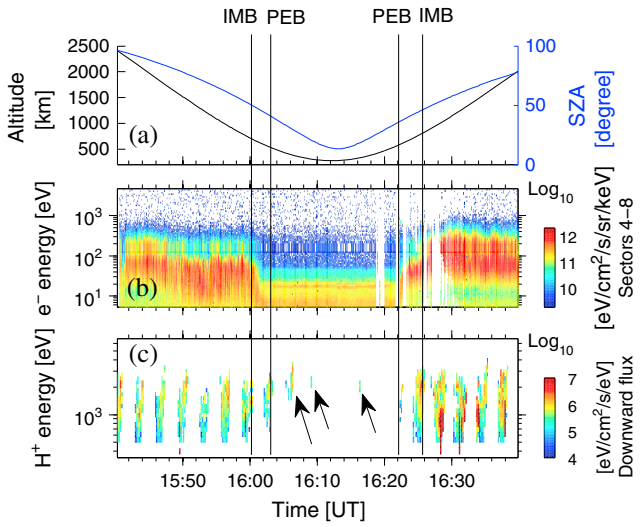

Figure 1. An example of proton penetration into the ionosphere. (a) Altitude (black solid line) and SZA (blue solid line) of Mars Express. (b) Electron energy-time spectrogram (the energy flux is averaged over sectors 4–8). The data gaps (white vertical bands) are an instrumental artifact. (c) Proton energy-time spectrogram (the energy flux is integrated over downgoing directions). The proton fluxes measured in the ionosphere are marked by arrows; they are referred to as "events." The vertical black lines indicate the PEB and IMB crossings.

The dayside ionosphere is identified by the CO_2 photoelectrons (horizontal line between 20–30 eV) between 1603 UT and 1621 UT. The "spot" shape of the proton energy distributions, occurring every 3 min in Figure 2c, is the result of the scanning in elevation angle of IMA. Several proton fluxes are observed within the ionosphere, at 1604–1607 UT, 1609–1610 UT, and 1616–1617 UT, and marked by arrows. During these three IMA scans, a part of the distribution is moving downward, i.e., precipitating. These three scans correspond to three events according to our definition of an event.

3. Spatial Distribution and Characteristics of the Events

[14] Figure 2a shows the number of IMA scans obtained below the local IMB in each spatial bin, excluding invalid data in the X_{MSO}-R_{MSO} plane. In the Mars Solar Orbital (MSO) Cartesian coordinate system, the X_{MSO} axis points from the center of Mars toward the Sun, the Y_{MSO} axis points opposite to the Martian orbital velocity vector and the Z_{MSO} axis completes the right-handed system. The total number of IMA scans (of 192 s time resolution) is 44,731. The coverage below the IMB is best at low altitudes around the terminator and poorer at the subsolar point and in the shadow. The altitude of the IMB changes with varying solar wind conditions, and it can be located above or below the position of the IMB model of *Dubinin et al.* [2006a], which is shown on the figure by a pink solid line. In Figures 2b, 2c, and 2d, we show only the spatial bins where the data coverage below the local IMB is at least 30 scans.

[15] We noticed that the proton events do not occur on every MEX orbit, so the question is how often we measure these events. Figure 2b shows the occurrence frequency of the observed events around Mars, calculated for each spatial bin, as the number of events divided by the number of IMA scans below the local IMB. We have found 524 events in total. The events are observed on the dayside ($X_{MSO} > 0$) and on the nightside ($X_{MSO} < 0$). The events extend from

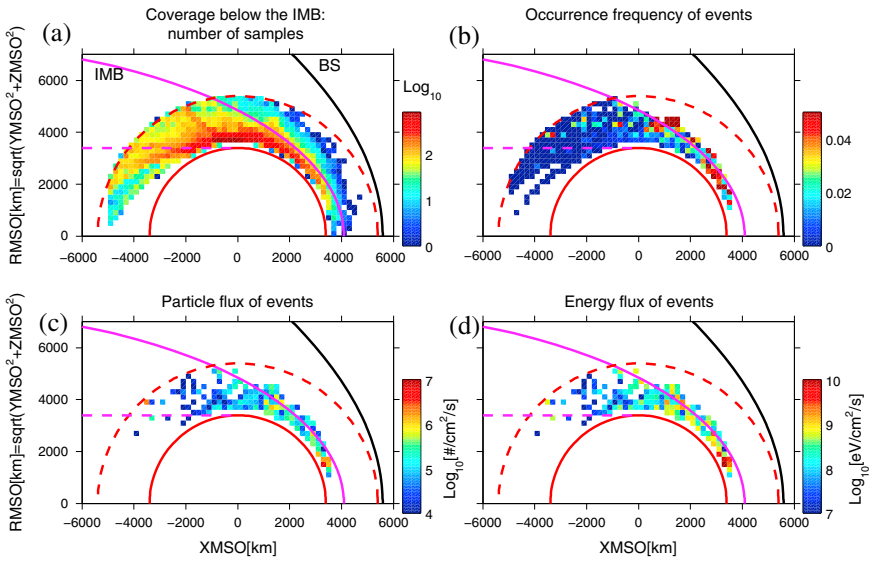

Figure 2. Each panel shows the X_{MSO}-R_{MSO} plane. The vertical axis is the distance $R_{MSO} = \sqrt{{Y_{MSO}}^2 + {Z_{MSO}}^2}$ from the Mars-Sun line. The spatial bin size is 200 km × 200 km. The red solid curve, the black solid curve, and the pink solid curve indicate: Mars, the bow shock model of *Vignes et al.* [2000] and the IMB model of *Dubinin et al.* [2006a]. The shadow region is represented below the pink dashed line. The red dashed curve shows the altitude limit of 2000 km, under which the data were taken. (a) Data coverage below the IMB. (b) Occurrence frequency of observing the events. (c) Average downward particle fluxes and (d) average downward energy fluxes of the events. See the text for details.

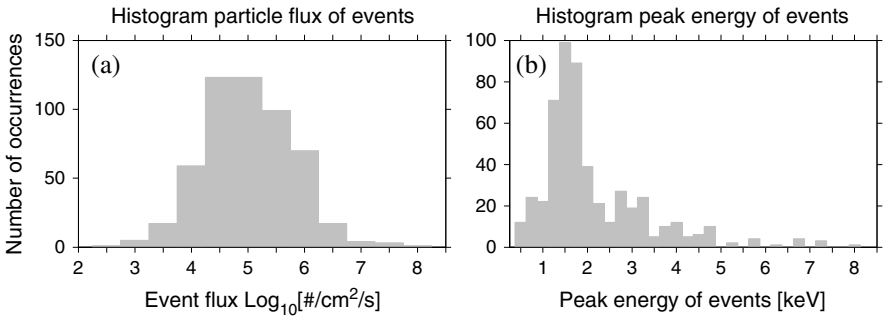

Figure 3. (a) Histogram of the downward particle flux of the events. (b) Histogram of the peak energy of the events.

the subsolar region up to 150° SZA. The solar wind void in the shadow of Mars is visible. The altitude spans from the pericenter (~260 km) up to the altitude limit that we have used of 2000 km. For the altitude distribution of the events, the median value is 608 km on the dayside, and 782 km on the nightside, respectively.

[16] Some events are found outside the position of the IMB model. These events are located in regions where the spacecraft is seldom below the local IMB so that the data coverage below the local IMB consists of less than 30 scans (which are thus not shown in the figure). In other words, in these regions the spacecraft is more often located in the magnetosheath than in the ionosphere. From Figure 2b, the occurrence frequency of observing the events is on average 3.2% on the dayside and 0.5% on the nightside outside the shadow. The low occurrence frequency in general indicates that the events are sporadic [see also *Diéval et al*., 2012b] and rare.

[17] Figures 2c and 2d show the average values of the downward particle fluxes and energy fluxes of the events in each spatial bin. Here and in the rest of the paper, we will consider the fluxes of the events (integrated over energy) when they occur and no occurrence frequency is taken into account, except when mentioned later in the paper. The particle and energy fluxes vary in the range 10^4–10^6 $cm^{-2}\,s^{-1}$ and 10^7–10^9 $eVcm^{-2}\,s^{-1}$, respectively. The geometric standard deviation, 10^(standard deviation($\log_{10}$(flux))), is a factor 6 for the particle fluxes and 7 for the energy fluxes. We made this choice for the error estimate because the flux values have a large dynamic range. The particle flux is higher on the dayside (median value $1.2 \cdot 10^5$ $cm^{-2}\,s^{-1}$) than on the nightside (median value $3.8 \cdot 10^4$ $cm^{-2}\,s^{-1}$). The flux decreases with increasing SZA. This trend is consistent with the results of hybrid modeling studies [*Kallio and Janhunen*, 2001; *Diéval et al*., 2012a]

[18] *Diéval et al*. [2012a] reported that the modeled precipitating flux decreases when altitude decreases at all SZA, with a more pronounced decrease in the subsolar region than at higher SZA. We note that the data coverage below the determined IMB is rather poor at low altitudes in the subsolar region (Figure 2c). The situation is better on the dayside flanks and there we see no altitude dependence of the downward flux of events. However, the figure presents all solar wind conditions mixed (the effect of which will be investigated in section 4), which makes the comparison difficult with a simulation that uses one set of solar wind parameters. Indeed, the events are collected below the IMB while the IMB altitude changes with upstream conditions, preventing us from seeing a eventual altitude dependence of the proton events in Figure 2.

[19] Figure 3a shows a histogram of the downward particle fluxes of events. The median value of the distribution is $9.8 \cdot 10^4$ $cm^{-2}\,s^{-1}$. Figure 3b shows a histogram of the peak energy of the events. We define the peak energy as the energy bin with the maximum differential flux in the energy spectrum. The events tend to have peak energies ≥ 1 keV. The mean and median values of the distribution are 2.1 and 1.7 keV, respectively. The distribution has a tail at high energies. The highest peak energy recorded is ~7.9 keV. However, the proton measurements are limited by an instrumental energy threshold depending on the PAC level in which IMA is run [*Barabash et al*., 2006]. The protons with energies < 1 keV require the highest PAC level to reach the detector. These low energy protons are not detected for the lowest PAC level. Therefore, the number of events with peak energies < 1 keV may be underestimated, and the determination of their peak energies may be less reliable, as the low-energy part of the energy spectrum would be cut-off. On the other hand, the events with peak energies ≥ 1 keV usually have their maximum fluxes at energies well above the energy threshold: their peak energies are reliable.

[20] As we have determined the peak energy of the events, we now look at the characteristics of the energy spectra. The energy spectra of the protons, integrated over downgoing directions, are sometimes broad in energy (several keV), but they typically have an energy width of ~0.5 keV.

[21] To obtain an average shape of the precipitating proton energy spectrum, we first shift the individual spectra to the mean peak energy of the events, 2.1 keV, and interpolate these spectra onto a linearly spaced energy grid between 0.6 and 10.0 keV with an energy step of 100 eV prior to averaging over the logarithm of the flux of all spectra. We note that such energy resolution is sufficient for resolving a spectrum with energy width ≥ 0.5 keV. The resulting average spectrum is shown in Figure 4. The spectrum is narrow in energy, in contrast to simulation results that show a broad energy range [*Brecht*, 1997; *Kallio and Janhunen*, 2001; *Diéval et al*., 2012a]. In addition, simulations by *Diéval et al*. [2012a] predict a low energy component (energy < 1 keV) in the precipitating proton spectrum, which we do not measure. One reason is that the instrumental energy cut-off of IMA, ~1.2 keV in the intermediate PAC level limits the detection of the low-energy protons.

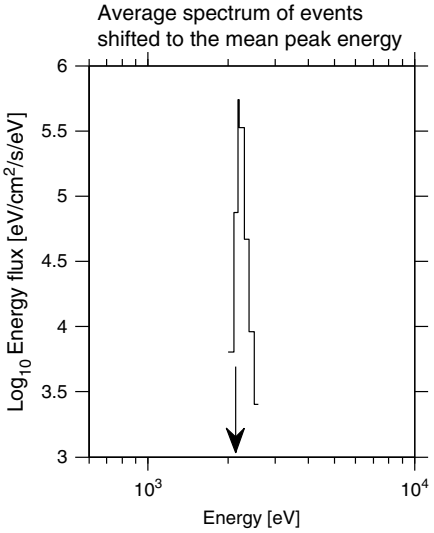

Figure 4. Spectrum of precipitating protons averaged over all individual event spectra, shifted to the mean peak energy of the events. Fluxes $<10^3$ eVcm^{-2} s^{-1} eV^{-1} are not shown. The arrow indicates the mean peak energy of the events.

[22] *Diéval et al.* [2012b] noted that the spectra of downgoing protons measured below the IMB become narrower in energy as the particles move through the pile-up region and enter the ionosphere. These authors report that the high-energy component of the original magnetosheath spectrum reaches low altitudes, while the low energy component vanishes at a higher altitude, likely due to deflection by the draped magnetic field. Thus, the statistical analysis confirms the tendency of the events to have narrow energy distributions peaking at high energies ≥ 1 keV (Figures 3b and 4).

4. Influence of Solar Wind Parameters, IMF Orientation, and Magnetic Anomalies

4.1. Influence of the Solar Wind Parameters

[23] In this section, we investigate how the proton precipitation is affected by the solar wind proton bulk velocity and by the magnetosheath proton temperature. For the solar wind velocity, we use moments taken when MEX is upstream of the bow shock model of *Vignes et al.* [2000]. For the magnetosheath temperature, we use moments taken when MEX is located between the previous bow shock model and the IMB model of *Dubinin et al.* [2006a]. An averaged-over-time value of the solar wind bulk velocity and magnetosheath temperature is attributed to each event provided that MEX spends some time in the magnetosheath and in the upstream solar wind on the inbound leg of the same orbit and that reliable moments are available. This procedure is not possible for all events because MEX does not enter the solar wind on every orbit. The magnetosheath temperature and the solar wind bulk velocity have been determined for 466 events and 271 events, respectively.

[24] Figure 5a shows histograms of the magnetosheath temperature. The grey shaded distribution corresponds to all magnetosheath temperature measurements from the studied period and the black shaded distribution corresponds to the magnetosheath temperature measurements estimated for the proton events. One sees that the distribution of the magnetosheath temperature of the events does not differ from the data of the studied period (Figure 5a). This indicates that the occurrence frequency of the events does not depend on the magnetosheath temperature. The median value of the magnetosheath temperature associated with the events is 50 eV.

[25] Figure 5c shows histograms of the solar wind speed. The grey shaded distribution corresponds to all solar wind speed measurements from the studied period and the black shaded distribution corresponds to the solar wind speed measurements estimated for the proton events. Figure 5c indicates that the events occur relatively more often during fast solar wind conditions (450–600 kms^{-1} bins) and less often during slow solar wind conditions (350 kms^{-1} bin), compared to the overall data from the studied period. The median value of the solar wind bulk velocity associated with the events is 434 kms^{-1}.

[26] Figure 5 (right column) shows the downward particle flux of the events as a function of the magnetosheath temperature and the solar wind bulk velocity. The plots indicate a large scatter of points. The downward flux has no clear correlation with either the solar wind velocity (Figure 5d) or the magnetosheath temperature (Figure 5b). There is a slight increase of the event flux with the magnetosheath temperature and with the solar wind velocity, but this trend is weak in relation to the significant scatter of the data points.

[27] Hybrid simulations predict an increase of the precipitating solar wind flux for increasing solar wind speed V and density n [*Brecht*, 1997]. It is generally assumed that the magnetic pressure $\sim B^2$ in the pile-up region counterbalances the upstream solar wind dynamic pressure $\sim nV^2$ (B = magnetic field strength). The magnetic pressure thus increases in the compressed pile-up region when Mars encounters a fast solar wind stream. In addition, a high-speed solar wind leads to shocked protons with high velocities v. In this case, the proton gyroradius mv/qB may not change much because both B and v have high values, while the size of the pile-up region is reduced. As a consequence, these protons are more likely to penetrate the thinner magnetic barrier without being backscattered; the fast solar wind can in principle enhance precipitation. The observed higher occurrence frequency of events for high solar wind speeds is consistent with this view. However, there is no clear correlation between the downward flux and the solar wind speed. This may be explained by the fact that the downward fluxes of the events can vary significantly during a given MEX orbit, even with steady solar wind conditions. The downward fluxes depend on several factors including the SZA and the distance reached by the protons below the IMB and this flux variability can cause the spread of data points in Figure 5d.

[28] In hot magnetosheath plasma, protons with large gyroradii may possibly pass through the magnetic barrier and precipitate due to a finite gyro radius effect. Thus, one can expect to obtain larger or more frequent downward flux when the magnetosheath plasma is hotter. However, there is no preferred occurrence of the events for a high magnetosheath temperature. This result may be due to the use of all upstream conditions, which may have different effects on the proton precipitation. For example, hot magnetosheath plasma can be caused by either a dense solar

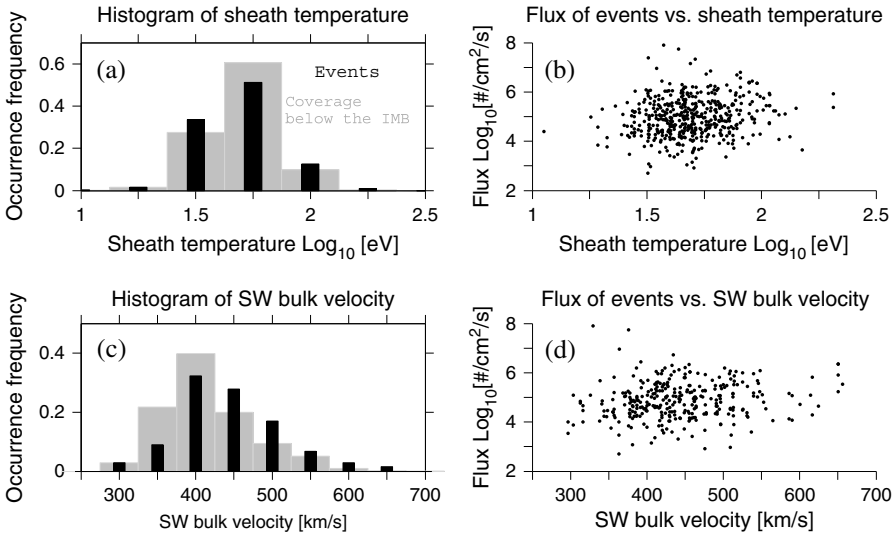

Figure 5. (a) Histograms of the magnetosheath proton temperature (see the text) (b) Downward event flux versus magnetosheath temperature. (c) Histograms of the solar wind bulk velocity (see the text). (d) Downward event flux versus solar wind proton bulk velocity. In Figures 5a and 5c, each distribution is normalized by the total number of samples of the population.

wind or a fast solar wind (high upstream dynamic pressure in both cases). The effect of the solar wind pressure pulses on the proton precipitation is left for a future study.

[29] High solar wind speeds and high magnetosheath temperatures are associated to populations of energetic protons. How does this relate to the peak energies of the events? Figure 6 shows the peak energy of the events as a function of the magnetosheath proton temperature (Figure 6a) and the solar wind bulk velocity (Figure 6b). We see that the peak energy range broadens toward higher energies both when the magnetosheath temperature increases and when the solar wind speed increases. This means that we find events that are more energetic when these parameters increase.

[30] Figure 7a shows the ratio of the downward particle flux of the events to the solar wind particle flux. The solar wind flux is calculated using the solar wind density and bulk velocity. From the figure, we see that some events (7 out of 271) have $\log_{10}(\text{ratio}) > 0$ (that is event flux > solar wind flux), which is due to an underestimation of the upstream flux. The flux of the cold solar wind beam can be underestimated due to field-of-view limitations, and also due to the energy cut-off of IMA. When ignoring these outliers, we obtain the median value of the distribution as equal to 0.002. Assuming that the precipitating protons come from the solar wind, this means that only very little of the solar wind flux is transmitted through the IMB when the precipitation occurs (0.2% on average). Considering that the events are observed during only ~3% of the observation time in the dayside ionosphere, we conclude that the particle input from the solar wind to the ionosphere, averaged over time, is not significant. Therefore, the Martian atmosphere is well protected by the magnetic barrier against the proton precipitation. For a comparison, *Diéval et al*. [2012a] find that 1% of the solar wind proton particle flux reaches 207 km altitude on the dayside of Mars, using a hybrid model. However, the proton precipitation is a recurrent phenomenon in such simulations [*Brecht*, 1997; *Kallio and Janhunen*, 2001; *Diéval et al*., 2012a]. Therefore, the previous modeling studies drastically overestimate the solar wind input to the atmosphere. This is partly because they have insufficient spatial resolution at low altitudes and because the ionosphere and atmosphere of these models are either not included or not realistic (for example the ionosphere is taken as a perfectly conductive sphere and collisions are not treated).

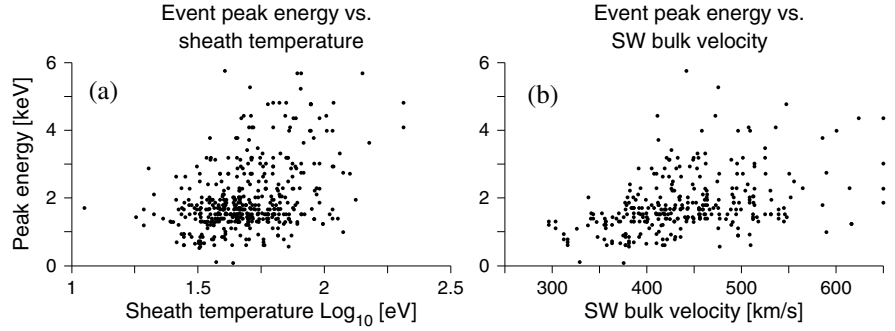

Figure 6. (a) Peak energy of the events versus magnetosheath proton temperature. (b) Peak energy of the events versus solar wind proton bulk velocity.

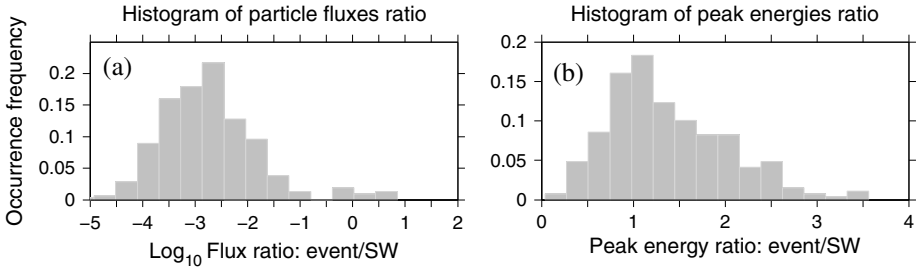

Figure 7. (a) Histogram of the downward proton particle flux ratio: event/solar wind. (b) Histogram of the proton peak energy ratio: event/solar wind. In both panels, each distribution is normalized by the total number of samples of the population.

The modeling of the interaction between the solar wind and the atmosphere/ionosphere is therefore inaccurate. This may lead the models to predict more solar wind entry than they should.

[31] It is also interesting to know how the peak energy of the events relates to the upstream peak energy. Figure 7b shows the ratio of peak energies between the events and the solar wind. The median value of the distribution is 1.2. The events tend to have their peak energy close to the upstream peak energy. The distribution has a tail toward ratios >1 and up to ~3.5. Exospheric proton picked up by the solar wind may obtain up to four times the solar wind proton mean energy. This is indeed also observed at Mars [e.g., *Dubinin et al*., 2006b; *Yamauchi et al*., 2006]. A ratio of up to 3.5 is thus consistent with such pick up, although we do not know how the bow shock would affect ions picked up in the solar wind. Hydrogen picked up in the magnetosheath should obtain lower energies due to lower flow speeds and a more magnetic field-aligned flow direction. Nevertheless, we cannot conclude whether the observed events have a solar wind origin or a planetary origin. *Diéval et al*. [2012b] reported that in their hybrid simulations the precipitating protons have both origins, with a larger proportion from the solar wind.

4.2. Influence of the IMF Orientation

[32] The solar wind convective electric field $\overrightarrow{E_{\mathrm{SW}}} = -\overrightarrow{V} \times \overrightarrow{B}$ controls the spatial deposition of the solar wind protons in hybrid simulations [*Brecht*, 1997; *Kallio and Janhunen*, 2001; *Diéval et al*., 2012a]. We will check this prediction by using our data.

[33] To determine the direction of $\overrightarrow{E_{\mathrm{SW}}}$ for the identified events, we use the magnetic field data from the MAG-ER instrument [*Acuña et al*., 1992] onboard the Mars Global Surveyor (MGS) spacecraft. The draped IMF orientation is assumed to be the same as in the upstream solar wind [*Brain et al*., 2006; *Fedorov et al*., 2006]. For minimizing the influence of the crustal fields, we only use magnetic field data recorded when MGS is on the dayside, between +50° and +60° latitudes [*Brain et al*., 2006]. For each event, we search whether there are data corresponding to this criterion in a time interval of 2 h before and after the event, and we average the direction of the magnetic field over time. The analysis of the effect of the IMF direction is possible until November 2006 (the end of the MGS mission). The IMF direction has been determined for 84 events.

[34] To study the effect of $\overrightarrow{E_{\mathrm{SW}}}$, we present the results in the Mars Solar Electric (MSE) frame. The MSE coordinate system is Cartesian: the X_{MSE} axis points from the center of Mars to the Sun, the Z_{MSE} axis is aligned with $\overrightarrow{E_{\mathrm{SW}}}$ and the Y_{MSE} axis completes the right-handed system. We define the $+\overrightarrow{E_{\mathrm{SW}}}$ hemisphere as the hemisphere where $\overrightarrow{E_{\mathrm{SW}}}$ points away from Mars ($Z_{\mathrm{MSE}} > 0$) and the $-\overrightarrow{E_{SW}}$ hemisphere as the hemisphere where $\overrightarrow{E_{\mathrm{SW}}}$ points toward Mars ($Z_{\mathrm{MSE}} < 0$).

[35] Figure 8 shows a view from the Sun in the MSE frame. Figure 8a shows the number of IMA scans below the IMB, excluding the invalid data. The data coverage is best around the terminator (where the black circle is located). In Figures 8b, 8c, and 8d, only the spatial bins where there are at least 30 IMA scans are used. The occurrence frequency for observing the events is shown in Figure 8b. The occurrence frequency is higher in the $-\overrightarrow{E_{SW}}$ hemisphere than in the $+\overrightarrow{E_{\mathrm{SW}}}$ hemisphere. In total, 34 events are found in the $+\overrightarrow{E_{\mathrm{SW}}}$ hemisphere, and 50 events are found in the $-\overrightarrow{E_{SW}}$ hemisphere. *Stenberg et al*. [2011] also find that solar wind origin alpha particles precipitating into the Martian ionosphere are detected more frequently in the $-\overrightarrow{E_{SW}}$ hemisphere than in the $+\overrightarrow{E_{\mathrm{SW}}}$ hemisphere.

[36] The downward particle flux of the events, averaged in each bin where the events occur, is shown in Figure 8c. The fluxes are higher in the $+\overrightarrow{E_{\mathrm{SW}}}$ hemisphere (median value $5.6 \cdot 10^5\,\mathrm{cm^{-2}\,s^{-1}}$, geometric mean value $1.2 \cdot 10^6\,\mathrm{cm^{-2}\,s^{-1}}$) than in the $-\overrightarrow{E_{SW}}$ hemisphere (median value $2.0 \cdot 10^5\,\mathrm{cm^{-2}\,s^{-1}}$, geometric mean value $1.9 \cdot 10^5\,\mathrm{cm^{-2}\,s^{-1}}$). The asymmetry is consistent with simulation studies [*Brecht*, 1997; *Kallio and Janhunen*, 2001; *Diéval et al*., 2012a]. Figure 8c considers the average fluxes when they occur. Figure 8d uses data from Figures 8b and 8c to show the averaged downward particle flux of the events multiplied by the occurrence frequency. The point of Figure 8d is to take into account the occurrence frequency of the proton events when considering the flux input to the ionosphere. This allows for direct comparisons with models where the proton precipitation occurs permanently. From Figure 8d, this flux corrected by occurrence frequency varies in the range 10^2–$10^4\,\mathrm{cm^{-2}\,s^{-1}}$. The discrepancy between modeled flux input and measured flux input is even worse in this case.

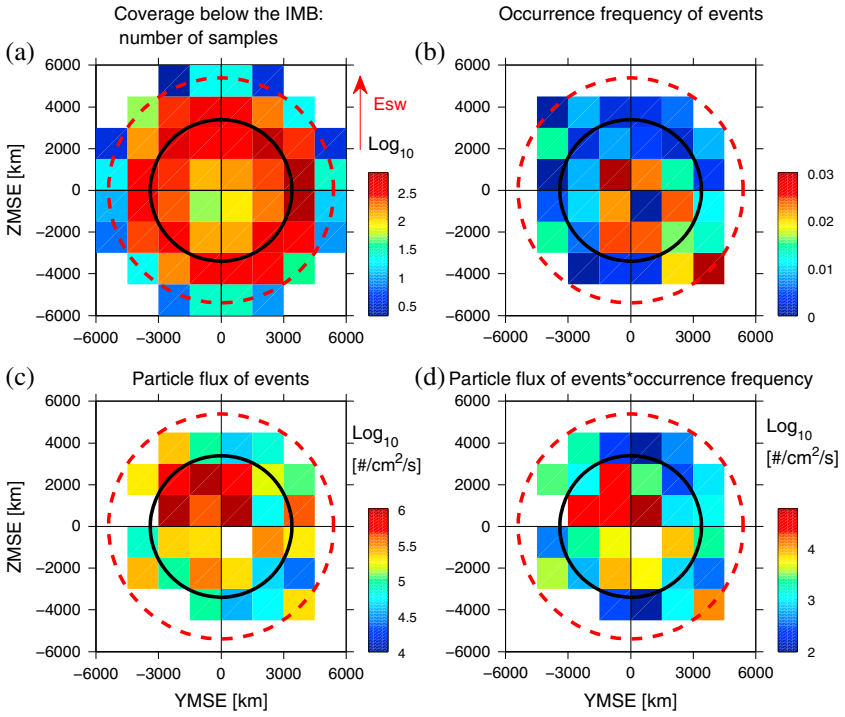

Figure 8. Each panel shows the Y_{MSE}-Z_{MSE} plane viewed from the Sun. The vertical axis points along the direction of the solar wind convective electric field. The spatial bin size is 1500 km × 1500 km. The solid black line indicates Mars, and the dashed red line indicates the altitude limit at 2000 km under which the data are taken. (a) Data coverage below the IMB. (b) Occurrence frequency of observing the events. (c) Average downward particle flux of the events. The average is made along the Mars-Sun line axis and includes both dayside and nightside. (d) Average downward particle flux of the events multiplied by the occurrence frequency of the events.

[37] Hybrid simulations predict that high-energy protons are deposited preferentially on the $+\vec{E}_{SW}$ hemisphere [*Brecht*, 1997; *Kallio and Janhunen*, 2001; *Diéval et al.*, 2012a]. Figure 9 shows a histogram of the peak energy of the events measured in the $+\vec{E}_{SW}$ hemisphere (grey shaded distribution) and in the $-\vec{E}_{SW}$ hemisphere (black shaded distribution). The mean and median value of the distribution are ~2.6 and ~1.9 keV, respectively, in the $+\vec{E}_{SW}$ hemisphere. The mean and median value of the distribution are ~1.9 and ~1.5 keV in the $-\vec{E}_{SW}$ hemisphere, respectively. Therefore, the events measured in the $+\vec{E}_{SW}$ hemisphere tend to be more energetic than in the $-\vec{E}_{SW}$ hemisphere, in reasonable agreement with the previous modeling studies. This result does not permit us to deduce the origin of the events. Indeed, hybrid simulations of precipitating proton patterns by *Diéval et al.* [2012a] show that both planetary proton and solar wind proton precipitation fluxes are larger in the $+\vec{E}_{SW}$ hemisphere than in the $-\vec{E}_{SW}$ hemisphere, although the asymmetry is less pronounced for the planetary protons.

4.3. Influence of the Crustal Magnetic Anomalies

[38] The crustal magnetic anomalies were discovered by MGS [*Acuña et al.*, 1998, 1999]. At 400 km altitude, the crustal magnetic field strength is < 50 nT in the northern hemisphere, while the strongest magnetic anomaly (field strength > 100 nT) is located in the southern hemisphere from 120°E to 240°E longitude and from –30° to –80° latitude.

[39] Simulation studies report that the solar wind protons may reach the Martian upper atmosphere preferably in regions of strong radial fields [*Harnett and Winglee*, 2006; *Brecht and Ledvina*, 2012]. Our data cover several Martian years; all solar effects (Martian season, solar wind and extreme ultraviolet (EUV) conditions, IMF orientation) should be eliminated when looking at the events in a longitude-latitude frame. Then, we can investigate the effect of the planetary crustal magnetic field on the events. We consider only observations at SZA < 45°, at altitudes below the local IMB, because the interaction between the crustal fields and the solar wind is assumed to be important in the subsolar region.

[40] In Figure 10a, we show the number of IMA scans below the IMB at SZA < 45°, excluding the invalid data. We use the planetocentric latitude and east longitude of the footprint of MEX. The data coverage is uneven in the southern hemisphere, with more data above the largest magnetic anomaly than elsewhere at the same latitude. This is because the data are collected below the local IMB, while the IMB rises in altitude above the strong southern crustal fields [e.g., *Crider et al.*, 2002].

[41] Figure 10b shows the occurrence frequency of observed events and Figure 10c shows the average downward particle flux of the events, in spatial bins of longitude and latitude, at SZA < 45°. The number of data samples in a given spatial bin is similar between the latitude band 0–60° of the

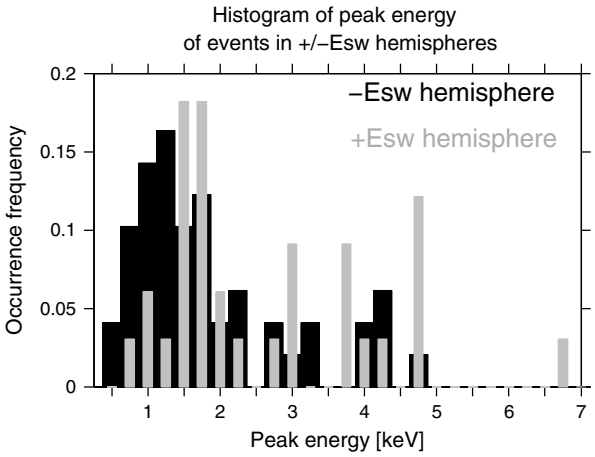

Figure 9. Histogram of the peak energies of the events in the $+\vec{E}_{SW}$ hemisphere (grey) and in the $-\vec{E}_{SW}$ hemisphere (black). Each distribution is normalized by the total number of samples of the population.

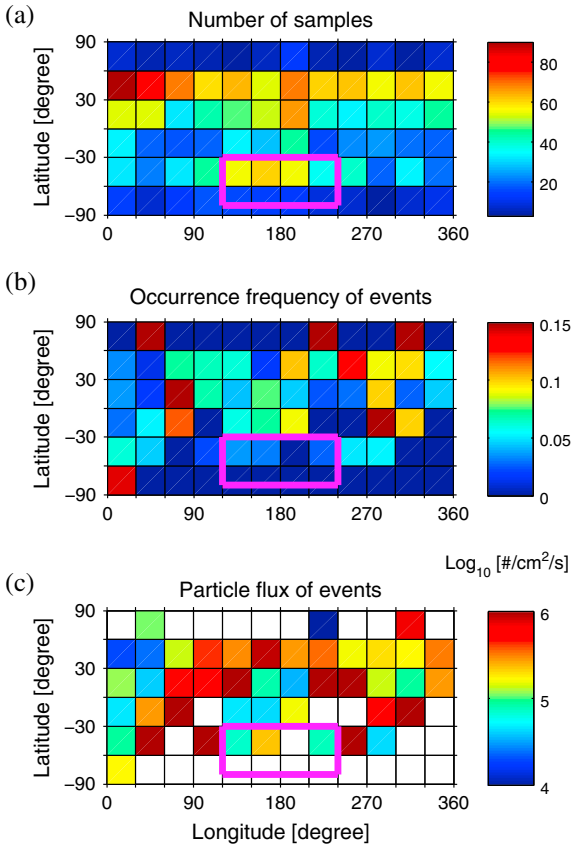

Figure 10. Each panel shows a map of the planetocentric longitude and latitude of MEX's footprint, for SZA < 45°. The bin size is 30° × 30°. The location of the strongest magnetic anomalies is delimited inside the thick pink solid rectangle. (a) Data coverage below the IMB. (b) Occurrence frequency of observing the events. (c) Average downward particle flux of the events. The white color means no event.

northern hemisphere and the region of the largest crustal fields (delimited by the pink rectangle). However, the occurrence frequency of the proton events (mean value 0.02) appears smaller above the largest crustal field than in the northern hemisphere (mean value 0.06). The average downward fluxes do not increase above the largest crustal fields, but are rather similar or even lower than the fluxes in the northern hemisphere. This means that the proton precipitation tends to decrease in regions of strong crustal field. We see no effect in regions of smaller crustal field, consistent with a case study by *Diéval et al.* [2012b]. On the other hand, *Stenberg et al.* [2011] reported no longitudinal dependence of the solar wind alpha particle precipitation. However, they used a shorter data period, including all dayside SZA and mix all latitudes, which may hide a possible dependence. Finally, our finding disagrees with the previous modeling work [*Harnett and Winglee*, 2006; *Brecht and Ledvina*, 2012]. A reason may be that we did not separate the regions of vertical and horizontal crustal fields in our work, because of the poor statistics.

[42] One can compare the gyroradius size of precipitating protons in different crustal field strengths. Typical energies for proton events are 1 keV. The gyroradius becomes 30 km for $B = 150$ nT (strong field at 400 km altitude), which is small compared to the gyroradius of 460 km for $B = 10$ nT (weak field at 400 km altitude). We interpret that the large

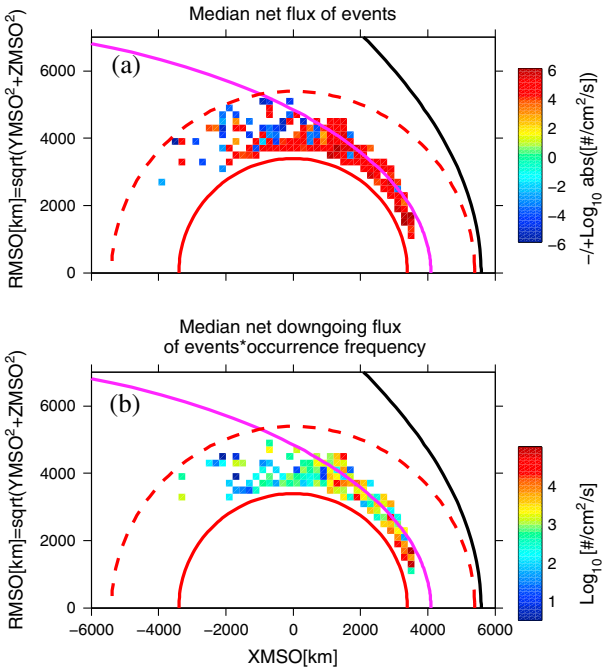

Figure 11. Each panel shows the X_{MSO}-R_{MSO} plane. The spatial bin size is 200 km × 200 km. The lines have the same format as in Figure 2. Only the spatial bins where the data coverage below the IMB comprises at least 30 scans are used. (a) Log_{10}(abs(median net flux of the events)), multiplied with a "–" ("+") sign for negative (positive) values of the median net flux. An upward (downward) net flux is negative (positive). (b) Median net particle flux of the events multiplied by their occurrence frequency, calculated only from the events with a net downward flux.

crustal fields are more effective at preventing the proton precipitation than the regions with weak field, by deflecting protons with small gyroradii.

5. Net Particle Input

[43] It is interesting to know whether the proton events have downward or upward net fluxes and how these fluxes are distributed in space. In this section, we calculate the net fluxes of the events through a spherical surface centered at Mars. For each event, the particle flux measured by a given energy channel, elevation angle and azimuth angle is multiplied by $\vec{s} \cdot \vec{a}$, where $\vec{s}$ is the nadir direction unit vector and $\vec{a}$ is the unit vector opposite to the viewing direction. This flux is then summed over all energy channels, elevation, and azimuth angles for the corresponding IMA scan. The net downward flux is positive, and the net upward flux is negative. We find that 136 events and 388 events have a net upward flux and net downward flux, respectively.

[44] Figure 11a shows the median net flux of the events in the X_{MSO}-R_{MSO} plane for the regions where the coverage (below the IMB and excluding invalid data) comprises at least 30 scans. We see that the net flux is downward close to Mars (red color) and upward or tailward further from Mars (blue color). This is particularly visible on the nightside. On the dayside, the events with a net upward flux are not obvious in the figure because they tend to be located at high altitudes in regions where the data coverage is seldom below the IMB (they are not shown in the figure). On the dayside, the median altitudes of the downward and upward net fluxes are 578 and 783 km, respectively. On the nightside, the median altitudes of the downward and upward net fluxes are 516 and 971 km, respectively. We will obtain a similar picture if we plot each event as an individual point colored by the net flux. The pattern is consistent with protons moving more toward the planet on the dayside and more tailward on the nightside, as the solar wind flows past the obstacle.

[45] Now, we will focus on the events that have a net downward flux. Figure 11b shows the median net downward flux multiplied by the occurrence frequency of these events. The flux tends to be larger on the dayside (10^2–10^4 cm^{-2} s^{-1}) than on the nightside (10^1–10^3 cm^{-2} s^{-1}).

[46] Then, we estimate the total net downward particle flux input through a half-sphere of radius $R_m + 578$ km on the dayside of Mars. $R_m = 3397$ km is the radius of Mars. We use the events having a net downward flux on the dayside; their median values of flux (corrected by occurrence frequency) and altitude are $\sim 1.2 \cdot 10^3$ cm^{-2} s^{-1} and 578 km, respectively (from Figure 11b). We calculate the total net downward flux through the half-sphere as follows: $1.2 \cdot 10^3 \cdot 2 \cdot \pi \cdot ((R_m + 578) \cdot 10^5)^2 = 1.2 \cdot 10^{21}$ s^{-1}. This is two orders of magnitude less than the number of solar wind protons precipitating at 207 km altitude on the dayside of Mars in the hybrid simulations by *Diéval et al.* [2012a]: $4.0 \cdot 10^{23}$ s^{-1}. For a comparison, we can calculate from the measurements, the median solar wind particle flux input through a disc of cross-section $\pi \cdot ((R_m + 578) \cdot 10^5)^2 cm^2$. We use the median solar wind particle flux associated with the events: $4.1 \cdot 10^7$ cm^{-2} s^{-1}. We obtain $4.1 \cdot 10^7 \cdot \pi ((R_m + 578) \cdot 10^5)^2 = 2.0 \cdot 10^{25}$ s^{-1}. Thus, the total net downward flux input from the events ($1.2 \cdot 10^{21}$ s^{-1}) corresponds to 0.006% of the upstream solar wind flux input.

6. Discussion and Conclusion

[47] We have conducted a statistical study of precipitating protons measured below the Martian IMB using Mars Express/ASPERA-3 data collected from February 2004 to April 2011, during the solar minimum.

[48] The observations of the downward proton events show an asymmetry relative to the solar wind convective electric field direction in terms of fluxes and peak energies, which is predicted by hybrid modeling studies [*Brecht*, 1997; *Kallio and Janhunen*, 2001; *Diéval et al.*, 2012a]. *Diéval et al.* [2012a] predicted fine spatial details in simulated proton precipitation maps. These details are not resolved by the observations of the events shown in MSE coordinates (Figure 8) for several reasons. First, the number of events must be high enough to provide good statistics everywhere around Mars. Additionally, there are not enough statistics to look at the events at different altitudes in the MSE system. We also need to know the orientation of the upstream IMF to organize the events according to the $\vec{E}_{SW}$, but Mars Express does not have a magnetometer. As mentioned above, we rely on MGS data to determine the IMF orientation. The operation of this mission ended in late 2006, reducing the number of events for which the IMF can be found.

[49] Proton precipitation events are observed during ~3% of the observation time when MEX is below the dayside IMB. This is in contrast to hybrid models, which predict that the proton precipitation occurs permanently. Why do we then observe so few events? Several reasons may lead to an underestimation of the number of events, and therefore of the occurrence frequency.

[50] The efficiency of the proton detection decreases below the IMA energy threshold: only the most energetic events can be detected when IMA is run in the lowest postacceleration level (this level was used for 5% of our data coverage). Furthermore, solar UV contamination was quite frequent during the ionospheric passes. The proton flux can be hard to separate from the instrumental noise, such that the events can be missed. Additionally, alpha particles can be detected in the proton channel if their flux is intense, leading to an overestimation of the proton fluxes: the corresponding events were discarded. We have removed 9058 invalid scans corresponding to 17% of the initial data coverage below the IMB (53789 scans). In addition, the region of major deposition of precipitating protons (where the precipitating flux is the highest) will change position as the upstream IMF direction changes. However, this seems not to be important for the probability of detecting the events because we see the events in both $\pm \vec{E}_{SW}$ hemispheres. Furthermore, the ion observations are made in situ, in only one location at a time. Therefore, it is possible that we miss events because we do not measure at the right place at the right time. This would be the case if the precipitation is a time-dependent process and if it occurs in spatially limited regions.

[51] Indeed, the observations of *Diéval et al.* [2012b] suggest that the precipitation is a dynamic phenomenon, which occurs only at times, most likely due to transients in the magnetosheath. This is consistent with the low occurrence frequency shown by the present study: the events are sporadic.

[52] The energy spectra of downward protons become narrower and restricted to relatively high energies, when

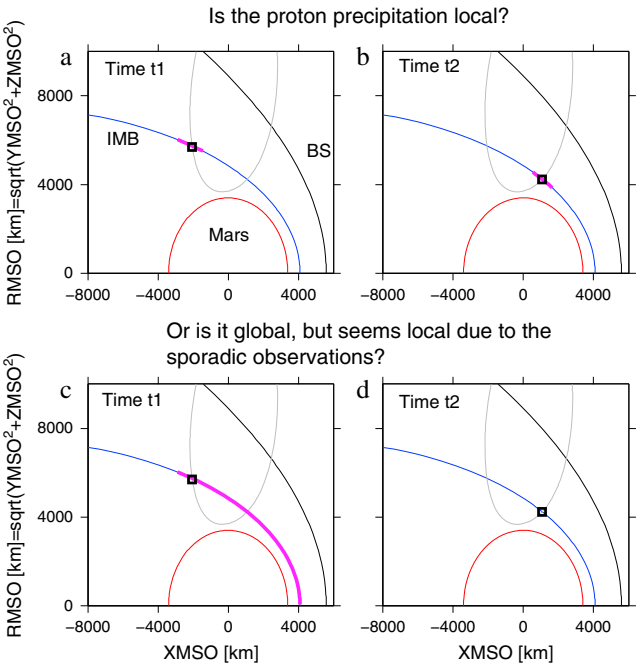

Figure 12. Each panel shows the X_{MSO}-R_{MSO} plane. The red, black, and blue solid line represent: Mars, the bow shock model of *Vignes et al*. [2000] and the IMB model of *Dubinin et al*. [2006a]. The grey solid line and the black square represent an orbit of MEX and the position of MEX at a given time, respectively. The thick pink solid line indicates a zone of proton precipitation. (a and b) Sketch proposed for a local precipitation, at times t1 and t2, respectively. (c and d) Sketch proposed for a global precipitation, at times t1 and t2, respectively.

the spacecraft moves from the magnetosheath to the ionosphere. Thus, protons at certain energies are "selected" to cross the magnetic barrier at certain times and enter the ionosphere. This may be caused by transient increases in the gyroradius of the magnetosheath proton population, such as measurable amounts of protons get a gyroradius large enough to cross the magnetic barrier. In the case of sporadic heating of the proton population, these protons with large gyroradii could in turn pass the magnetic barrier, as observed.

[53] The minimum precipitating proton flux that is detected is of the order of 10^{-4} of a typical magnetosheath proton flux and corresponds to the high-energy tail of the magnetosheath spectrum. A precipitating flux is assumed undetected if it is smaller than 10^{-4} of the magnetosheath flux. We consider a Maxwellian distribution of temperature 50 eV and density 3 cm^{-3} for the magnetosheath. We estimate that a temperature increase of ~15 eV permits to increase by one order of magnitude the precipitating proton flux, to a measurable minimum level of 10^{-4} of the magnetosheath flux, for energies above a given threshold (value is not important). This is possible due to the increase in thermal spread of the magnetosheath distribution, leading to higher fluxes for the high energy tail.

[54] A question that remains is what is the typical size of a region of proton precipitation? Hybrid modeling studies [*Brecht*, 1997; *Kallio and Janhunen*, 2001; *Diéval et al*., 2012a] predict that the protons precipitate over a large area of the planet. A case study by *Diéval et al*. [2012b] reports that precipitating protons have been measured below the IMB over a distance of ~4000 km along an orbit of MEX. In our statistical analysis, precipitation events were detected on 363 MEX orbits out of 4707 orbits (8% of the orbits). On one hand, 256 out of 363 orbits counted just one event, suggesting a small precipitation area. On the other hand, 2 out of 363 orbits counted 6 events, suggesting a rather large precipitation area. Note that the spacecraft covers a distance of ~768 km near pericenter during a full IMA scan of 192 s. There is in any case a trend to see the precipitation only for a short time.

[55] Figure 12 shows a sketch of the sporadic precipitation, as it could be observed by MEX at two times t1 and t2 (left and right columns, respectively). Figures 12a and 12b illustrate an example of local precipitation in a small area, which will be detected if MEX is at the right place at the right time. Figures 12c and 12d illustrate a global precipitation in an extended area, which will appear as local if it is intermittent. The question of the size of the precipitation region could be solved with two hypothetical orbiters flying over the same region. The imaging of the spatial distribution of hydrogen energetic neutral atoms (H ENAs), backscattered by the atmosphere, would also help to obtain a picture of the proton precipitation [*Futaana et al*., 2006]. These H ENAs are generated through charge exchange reactions between cold planetary atoms and solar wind protons in the vicinity of Mars [*Kallio et al*., 1997; *Kallio and Barabash*, 2001; *Holmström et al*., 2002].

[56] The events intermittently bring particle fluxes in the range 10^4–10^6 cm^{-2} s^{-1} into the atmosphere. These fluxes are two orders of magnitude lower than the modeled precipitating fluxes calculated by *Kallio and Janhunen* [2001]. In contrast, the measured fluxes vary within the range of the modeled precipitating fluxes calculated at 260 km altitude by *Diéval et al*. [2012a], but they are one order of magnitude lower than the modeled fluxes calculated at 560 km altitude. Therefore, the quantitative comparison with the models is not simple, as the different models have different input parameters and set ups. The way the models treat the ionosphere/atmosphere may be responsible for a part of the discrepancy between modeled and measured fluxes.

[57] Does the precipitating proton energy flux play any role in the heating of the upper atmosphere? The energy fluxes measured on the dayside (10^8–10^9 eVcm^{-2} s^{-1}) are much lower than the heat input from the solar radiation absorption at Mars for solar minimum conditions (height-integrated between 100–240 km) from *Kallio et al*. [1997]: $1.35 \cdot 10^{11}$ eVcm^{-2} s^{-1}. The proton precipitation thus has a minor role in the heat balance on the dayside, compared to the solar EUV. On the other hand, precipitation events have been measured also on the nightside in the absence of solar radiation. Although they are even less frequent than the dayside events, they carry an energy flux of 10^7–10^8 eVcm^{-2} s^{-1}, which is significant in the absence of EUV.

[58] The precipitating proton fluxes can also be compared to the fluxes of penetrating solar wind electrons observed by *Dubinin et al*. [2008] in the energy range 40–80 eV. *Dubinin et al*. [2008] reported that the maximum solar wind electron particle flux can reach 10^{10} cm^{-2} s^{-1} on the dayside and can reach $>10^9$ cm^{-2} s^{-1} as spikes on the nightside. This gives an order of magnitude for the energy flux, 10^{11} eVcm^{-2} s^{-1} on the dayside and $>10^{10}$ eVcm^{-2} s^{-1} as spikes on the nightside. *Dubinin*

et al. [2008] estimated that these electron spikes increase the ionization and are needed for causing aurora on the nightside. For comparison with the solar wind electrons, our maximum proton energy fluxes are two orders of magnitude lower on the dayside and the nightside. Thus, the local ionization effect of the proton events is negligible compared to the ionization due to the solar wind electrons. It is also unlikely that the proton events are a driver for aurora, in contrast with estimations of *Kallio and Janhunen* [2001].

[59] In conclusion, the statistical study of the precipitating proton events confirms that the proton precipitation, likely driven by the gyroradius effect, does exist on Mars, on the dayside and the nightside. The energy distributions of the events correspond to the high-energy part of the magnetosheath proton distribution (~keV energy), which is able to penetrate the magnetic barrier due to large gyroradii. The events are rare (~3% of the observation time on the dayside). The precipitation is more frequent during periods of fast solar wind than during periods of slow solar wind. Transients in the magnetosheath may explain the intermittence of the events. The study confirms the asymmetry related to the solar wind convective electric field reported by hybrid models. The strongest magnetic anomalies tend to locally reduce the proton precipitation. The events carry ~0.2% of the upstream solar wind flux on average when they occur, which indicates that the magnetic barrier effectively shields the upper atmosphere against the incident magnetosheath protons. On the dayside, the resulting heating and ionization of the upper atmosphere are insignificant compared to the solar EUV flux. On the nightside, the heating and ionization are minor compared to the effects of the solar wind electrons on the ionosphere. The median net input of the precipitating proton particle flux to the dayside ionosphere, corrected by occurrence frequency, is estimated as $1.2 \cdot 10^{21}$ s^{-1}.

[60] The present study covers the solar minimum. A future goal would be to study the proton precipitation during the coming solar maximum and to compare these data with those obtained during the solar minimum. The production rate of planetary O^+ ions is expected to be more important during the solar maximum than the solar minimum because of increased neutral oxygen densities and because of increased UV radiation. According to hybrid simulations [*Kallio and Janhunen*, 2001], the proton precipitation decreases when the O^+ production rate increases. This result shall be compared with the observations.

[61] **Acknowledgments.** C. D. and G. S. are supported by the National Graduate School of Space Technology of the Luleå Technical University. C. D. acknowledges funding from the Kungliga Vetenskapsakademien. The Swedish contribution to the ASPERA-3 experiment is supported by the Swedish National Space Board. C. D. thanks Markus Fränz from the Max-Planck Institut für Sonnensystemforschung (Katlenburg-Lindau) for providing the IMA moments used in this study.

References

Acuña, M. H., et al. (1992), Mars Observer magnetic field investigations, *J. Geophys. Res.*, *97*(E5), 7799–7814.

Acuña, M. H., et al. (1998), Magnetic field and plasma observations at Mars: Preliminary Results of the Mars Global Surveyor Mission, *Science*, *279*(5357), 1676–1680, doi:10.1126/science.279.5357.1676.

Acuña, M. H., et al. (1999), Global distribution of crustal magnetization discovered by the Mars Global Surveyor MAG/ER experiment, *Science*, *284*(5415), 790–793, doi:10.1126/science.284.5415.790.

Barabash, S., et al. (2006), The Analyzer of Space Plasmas and Energetic Atoms (ASPERA-3) for the Mars Express Mission, *Space Sci. Rev.*, *126*(1–4), 113–164, doi:10.1007/s11214-006-9124-8.

Brain, D. A., et al. (2006), Magnetic field draping direction at Mars from April 1999 through August 2004, *Icarus*, *182*, 464–473, doi:10.1016/j.icarus.2005.09.023.

Brecht, S. H. (1997), Solar wind proton deposition into the Martian atmosphere, *J. Geophys. Res.*, *102*(A6), 11,287–11,294, doi:10.1029/97JA00561.

Brecht, S. H., and S. A. Ledvina (2012), Control of ion loss from Mars during solar minimum, *Earth Planets Space*, *64*, 165–178, doi:10.5047/eps.2011.05.037.

Crider, D. H., et al. (2002), Observations of the latitude dependence of the location of the martian magnetic pileup boundary, *Geophys. Res. Lett.*, *29*, 11–1, doi:10.1029/2001GL013860.

Diéval, C., et al. (2012a), Hybrid simulations of proton precipitation patterns onto the upper atmosphere of Mars, *Earth Planets Space*, *64*, 121–134, doi:10.5047/eps.2011.08.015.

Diéval, C., et al. (2012b), A case study of proton precipitation at Mars: Mars Express observations and hybrid simulations, *J. Geophys. Res.*, *117*, A06222, doi:10.1029/2012JA017537.

Dubinin, E., et al. (2006a), Plasma Morphology at Mars. Aspera-3 Observations, *Space Sci. Rev.*, *126*, 209–238, doi:10.1007/s.11214-006-9039-4.

Dubinin, E., et al. (2006b), Hydrogen exosphere at Mars: pickup protons and their acceleration at the bow shock, *Geophys. Res. Lett.*, *33*, L22103, doi:10.1029/2006GL027799.

Dubinin, E., et al. (2008), Access of solar wind electrons into the Martian magnetosphere, *Ann. Geophys.*, *26*, 3511–3524, doi:10.5194/angeo-26-3511-2008.

Fedorov, A., et al. (2006), Structure of the martian wake, *Icarus*, *182* (2), 329–326, doi:10.1016/j.icarus.2005.09.021.

Frahm, R. A., et al. (2006), Carbon dioxide photoelectron energy peaks at Mars, *Icarus*, *182*(2), 371–382, doi:10.1016/j.icarus.2006.01.014.

Fränz, M., et al. (2006), Plasma moments in the environment of Mars: Mars Express ASPERA-3 observations, *Space Sci. Rev.*, *126*, 165–207, doi:10.1007/s11214-006-9115-9.

Futaana, Y., et al. (2006), First ENA observations at Mars: ENA emissions from the Martian upper atmosphere, *Icarus*, *182*(2), 424–430, doi:10.1016/j.icarus.2005.09.019.

Harnett, E. M., and R. M. Winglee (2006), Three-dimensional multifluid simulations of ionospheric loss at Mars from nominal solar wind conditions to magnetic cloud events, *J. Geophys. Res.*, *111*(A9), A09213, doi:10.1029/2006JA011724.

Holmström, M., et al. (2002), Energetic neutral atoms at Mars 1 Imaging of solar wind protons, *J. Geophys. Res.*, *107*(A10), 1277, doi:10.1029/2001JA000325.

Kallio, E., et al. (1997), Charge exchange near Mars: the solar wind absorption and energetic neutral atom production, *J. Geophys. Res.*, *102*(A10), 22,183–22,197, doi:10.1029/97JA01662.

Kallio, E., and S. Barabash (2000), On the elastic and inelastic collisions between precipitating energetic hydrogen atoms and Martian atmospheric neutrals, *J. Geophys. Res.*, *105*(A11), 24,973–24,996, doi:10.1029/2000JA900077.

Kallio, E., and S. Barabash (2001), Atmospheric effects of precipitation energetic hydrogen atoms on the martian atmosphere, *J. Geophys. Res.*, *106*(A1), 165–177, doi:10.1029/2000JA002003.

Kallio, E., and P. Janhunen (2001), Atmospheric effects of proton precipitation in the Martian atmosphere and its connection to the Mars-solar wind interaction, *J. Geophys. Res.*, *106*(A4), 5617–5634, doi:10.1029/2000JA239.

Lundin, R., et al. (2004), Solar wind-induced atmospheric erosion at Mars: first results from ASPERA-3 on Mars Express, *Science*, *305*(5692), 1933–1936, doi:10.1126/science.1101860.

McNeal, R. J., and D. C. Clark (1969), Ionization and Excitation of Nitrogen by Protons and Hydrogen Atoms in the Energy Range 1-25 kev, *J. Geophys. Res.*, *74*(21), 5065–5072, doi:10.1029/JA074i021p05065.

Nagy, A. F., et al. (2004), The plasma environment of Mars, *Space Sci. Rev.*, *111*, 33–114, doi:10.1023/B:SPAC.0000032718.47512.92.

Shematovich, V. I., et al. (2011), Protons and hydrogen atoms transport in the Martian upper atmosphere with an induced magnetic field, *J. Geophys. Res.*, *116*, A11320, doi:10.1029/2011JA017007.

Stebbings, R. F., et al. (1964), Charge Transfer between Oxygen Atoms and O^+ and H^+ Ions, *J. Geophys. Res.*, *69*(11), 2349–2355, doi:10.1029/JZ069i011p02349.

Stenberg, G., et al. (2011), Observational evidence of alpha particle capture at Mars, *Geophys. Res. Lett.*, *38*, L09101, doi:10.1029/2011GL047155.

Vignes, D., et al. (2000), The solar wind interaction with Mars: Locations and shapes of the Bow Shock and the magnetic pile-up boundary from the observations of the MAG/ER experiment onboard Mars Global Surveyor, *Geophys. Res. Lett.*, *27*, 49–52, doi:10.1029/1999GL010703.

Yamauchi, M., et al. (2006), IMF direction derived from cycloid-like ion distributions observed by Mars Express, *Space Sci. Rev.*, *126*, 239–266, doi:10.1007/s11214-006-9090-1.